

Graphene wrapped NASICON-type $\text{Fe}_2(\text{MoO}_4)_3$ nanoparticles as a ultra-high rate cathode for sodium ion batteries



Jinzhi Sheng^{a,1}, Han Zang^{a,1}, Chunjuan Tang^{a,b,1}, Qinyou An^{a,*}, Qiulong Wei^a,
Guobin Zhang^a, Lineng Chen^a, Chen Peng^a, Liqiang Mai^{a,*}

^a State Key Laboratory of Advanced Technology for Materials Synthesis and Processing, Wuhan University of Technology, Luoshi Road 122, Wuhan 430070, PR China

^b Department of Mathematics and Physics, Luoyang Institute of Science and Technology, Luoyang 471023, PR China

ARTICLE INFO

Article history:

Received 21 January 2016

Received in revised form

1 April 2016

Accepted 13 April 2016

Available online 26 April 2016

Keywords:

$\text{Fe}_2(\text{MoO}_4)_3$

NASICON

Micro-emulsion

High rate

Sodium ion battery

ABSTRACT

Na^+ superionic conductor (NASICON) type $\text{Fe}_2(\text{MoO}_4)_3$ with capacious ion diffusion tunnels and a flat discharge plateau, is a promising cathode material for sodium ion batteries. However, the sluggish electrochemical kinetics limits its further development due to the poor electron conductivity and long Na^+ diffusion path. In this work, a graphene wrapped $\text{Fe}_2(\text{MoO}_4)_3$ nanoparticle composite was synthesized via a micro-emulsion method followed by annealing. The composite exhibits ultra-high rate capability (64.1 mA h g^{-1} at 100 C, better than all the reported works) and good high-rate cycling stability (76% capacity retention after 100 cycles at 10 C). The enhanced electrochemical performances are attributed to the unique composite structure with shortened ion diffusion distance and high electron conductivity. Furthermore, the Na^+ insertion/extraction mechanism of the composite is systematically investigated, based on *in-situ* X-ray diffraction (XRD) and X-ray photoelectron spectroscopy (XPS). Our work demonstrates that the graphene wrapped $\text{Fe}_2(\text{MoO}_4)_3$ nanoparticle composite has great potential for high-rate sodium ion batteries.

© 2016 Elsevier Ltd. All rights reserved.

1. Introduction

With the insufficiency of lithium, lithium ion batteries (LIBs) can hardly meet the worldwide sustaining demand [1–5]. As a candidate, sodium ion batteries (SIBs) hold great promise to be the next generation of energy storage devices due to the high abundance of sodium and the similarity of its electrochemical mechanism to that of LIBs [6–8]. However, the larger ionic radius of Na^+ (0.98 Å) in comparison with that of Li^+ (0.69 Å) causes the lower Na^+ diffusion coefficient and larger volume change, resulting in poor rate and cycling performances [9–13]. Unfortunately, some materials such as layered Na_xCoO_2 and olivine-type NaFePO_4 , being primarily and widely considered for SIBs due to the success of their analog LiCoO_2 and LiFePO_4 , failed to overcome the inherent limitations of SIBs on account of the narrow ion diffusion tunnels and the irreversible phase transition after Na^+ intercalation [14–17]. Therefore, new cathode materials with suitable structures for Na^+ intercalation are urgently required to be exploited for SIBs.

Na^+ superionic conductor (NASICON) with an ideal open three-dimensional (3D) framework for Na^+ transportation, has been regarded as the optimal cathode material for SIBs [18–20]. Among these NASICON-type materials, only a few possess electrochemical activity, and iron molybdate ($\text{Fe}_2(\text{MoO}_4)_3$) is one of them [21]. As a cathode material for SIBs, $\text{Fe}_2(\text{MoO}_4)_3$ is nontoxic and has a flat discharge voltage plateau ($\sim 2.6 \text{ V}$ versus Na^+/Na), which shows great prospect for sodium ion storage [22]. Nevertheless, its further development is limited by the sluggish electrochemical kinetics caused by the poor electronic conductivity and the long Na^+ diffusion path [22–26]. Compositing electrode active material with conductive agents is an effective approach to enhance the electronic conductivity [27–28]. Nguyen *et al.* mixed $\text{Fe}_2(\text{MoO}_4)_3$ with several conductive agents such as nanosilver [23], carbon nanotubes [24] and reduced graphene oxide [25], and the electronic conductivities of the products are indeed higher than that of the pure $\text{Fe}_2(\text{MoO}_4)_3$. However, the capacity of $\text{Fe}_2(\text{MoO}_4)_3$ /reduced graphene oxide composite, the best one among the three products, decreased to lower than 80 mA h g^{-1} (90.6 mA h g^{-1} at 0.1 C) when the charging–discharging rate reached 1.5 C, which may be due to the large sizes of the $\text{Fe}_2(\text{MoO}_4)_3$ particles [25]. So far, high rate $\text{Fe}_2(\text{MoO}_4)_3$ cathode material has not been reported. Thus, low rate capability severely limits the further development of $\text{Fe}_2(\text{MoO}_4)_3$. Reducing the sizes of the active material is an

* Corresponding authors.

E-mail addresses: anqinyou86@whut.edu.cn (Q. An), mlq518@whut.edu.cn (L. Mai).

¹ These authors contributed equally to this work.

effective way to improve the rate capability, because nanostructures can provide larger electrode/electrolyte contact area and shorter distance for ion transport [29–31]. Therefore, to obtain high performance $\text{Fe}_2(\text{MoO}_4)_3$ cathode material, compositing with conductive agents and reducing the sizes of the particles should be simultaneously achieved.

Herein, we report a graphene wrapped $\text{Fe}_2(\text{MoO}_4)_3$ nanoparticle composite synthesized via a micro-emulsion method followed by annealing. As a cathode material for SIBs, the graphene wrapped $\text{Fe}_2(\text{MoO}_4)_3$ nanoparticle composite exhibits high rate capability (64.1 mA h g^{-1} at 100 C) and good high-rate cycling stability (more than 76% capacity retention after 100 cycles at 10 C). The improvement of the electrochemical performance can be attributed to the synergetic advantages of the nano-sized $\text{Fe}_2(\text{MoO}_4)_3$ particles and the high-conductive graphene, which provide not only shortened Na^+ diffusion path but also effective electron transportation. Furthermore, the Na^+ insertion/extraction mechanism of the composite is systematically investigated by *in-situ* X-ray diffraction (XRD) and X-ray photoelectron spectroscopy (XPS).

2. Experimental section

All the reagents used in the experiment were of analytical grade and used without further purification.

2.1 Sample preparation

For a typical synthesis, $\text{Fe}_2(\text{MoO}_4)_3$ nanoparticles were synthesized by a micro-emulsion method followed by annealing process. 0.4 g sodium dodecyl sulfate (SDS) was dissolved in a mixture of 20 mL of cyclohexane and 20 mL cyclohexanol, which was subsequently stirred for 30 min. After that, 15 mL $\text{Fe}(\text{NO}_3)_3$ aqueous solution (0.093 M) and 15 mL $(\text{NH}_4)_6\text{Mo}_7\text{O}_{24}$ aqueous solution (0.020 M) were added into the above solution. Then the suspension was stirred for another 1.5 h. This precursor was collected by centrifugation and washed with deionized water and ethanol for several times, and dried at 70 °C for 12 h in air. Then, the precursor was annealed in air at 500 °C for 2 h to obtain the $\text{Fe}_2(\text{MoO}_4)_3$ nanoparticles (FMO-M).

The graphene was synthesized by a modified Hummers method [28–29]. To obtain the graphene wrapped $\text{Fe}_2(\text{MoO}_4)_3$ nanoparticles (noted as FMO-MG), 0.15 g FMO-M were dispersed in water by an ultrasonic process. Then 6 mL of graphene ($\sim 1.8 \text{ g L}^{-1}$) solution was added into the suspension and the mixture was stirred for 12 h. The final product was collected by centrifugation and dispersed in pure alcohol, and then dried at 70 °C in air for 12 h.

To further analyze the relationship between the structure and performance, a control sample was synthesized via a hydrothermal method. 25 mL $(\text{NH}_4)_6\text{Mo}_7\text{O}_{24}$ (0.06 M) aqueous solution and 20 mL NH_4NO_3 aqueous solution (0.45 M) were mixed with stirring. Then 25 mL $\text{Fe}(\text{NO}_3)_3$ aqueous solution (0.28 M) was added into the above solution under magnetic stirring at room temperature. The resulting suspension was transferred into a 100 mL Teflon-lined stainless steel autoclave. The autoclave was heated at 180 °C for 12 h, and then cooled to room temperature naturally. The precipitate was washed several times with distilled water and ethanol, respectively. Finally the product (noted as FMO-H) was obtained after dried in a vacuum at 70 °C for 12 h.

To obtain the carbon nanotubes (CNTs) wrapped $\text{Fe}_2(\text{MoO}_4)_3$ nanoparticles (noted as FMO-CNTs), 0.15 g FMO-M were dispersed in water by an ultrasonic process. Then 10.8 mg CNTs and 6 mL water were added into the suspension and the mixture was stirred for 12 h. The final product was collected by centrifugation and dispersed in pure alcohol, and then dried at 70 °C in air for 12 h.

2.2 Materials characterization

X-ray diffraction (XRD) and *in-situ* XRD measurements were performed to investigate the crystallographic information using a Bruker D8 Advance X-ray diffractometer with a non-monochromated Cu K α X-ray source. Scanning electron microscopy (SEM) images and energy dispersive X-ray spectra (EDS) were collected with a JEOL-7100F SEM/EDS microscope at an acceleration voltage of 20 kV. Transmission electron microscopy (TEM) and high resolution transmission electron microscopy (HRTEM) images were recorded by using a JEM-2100F STEM/EDS microscope. Bräuauer–Emmerr–Teller surface areas were measured using a Tristar II 3020 instrument by adsorption of nitrogen at 77 K. XPS measurement was performed using a VG Multi Lab 2000 instrument. Raman spectra were acquired using a Renishaw RM-1000 laser Raman microscopy. Thermogravimetry (TG) was performed using a Netzsch STA 449 C simultaneous thermal analyzer at a heating rate of 10 °C min^{-1} in air.

2.3 Measurements of electrochemical performances

The electrochemical properties were measured with 2016 coin cells assembled in a glove box filled with pure argon gas. In sodium half cells, sodium metal was used as the anode. 1 M solution of NaClO_4 in ethylene carbon (EC)–dimethyl carbonate (DMC) (1:1 w/w) was used as the electrolyte. The electrodes were produced from a mixed clay with a weight ratio of 60% $\text{Fe}_2(\text{MoO}_4)_3$ /graphene active material, 30% acetylene black and 10% PTFE. The mixed clay was rolled using a roller mill to form a freestanding film and the film was cut into slices and dried. The loading mass of the active material in each electrode slice was 1.5–3.0 mg. Galvanostatic charge–discharge measurement was performed in the potential range of 1.5–4.0 V versus Na^+/Na with a multi-channel battery testing system (LAND CT2001A). Cyclic voltammetry (CV) curves and electrochemical impedance spectra (EIS) were recorded with an electrochemical workstation under the alternating current ranging from 0.01 Hz to 10 kHz (CHI 760D and Autolab PGSTAT 302).

3. Results and discussions

The formation process of the graphene wrapped $\text{Fe}_2(\text{MoO}_4)_3$ nanoparticle composite is illustrated in Fig. 1. The possible formation mechanism of the nanowire precursor can be understood in a micro-emulsion based synthesis [32]. Initially, the hydrophilic solutes (Fe^{3+} and MoO_4^{2-}) are dispersed into droplets by the oil phases [33–34]. By stirring, continuous coalescence and breakup occur between the droplets, during which the reactants in the individual droplets can come in close contact for precipitation reaction [35–36]. This process just takes a few seconds, and was summarized as a collision mechanism [36–37]. Then, the precipitate started nucleating and growing, resulting in uniform nanowire precursor due to the preferential adsorption of surfactant sodium dodecyl sulfate (SDS) [38–39]. The SEM images of products after different stirring time of 10, 30 and 60 min (Fig. S1) provide an evidence for the growing process of the nanowire precursor. No obvious diffraction peak can be detected in the XRD pattern, indicating that the precursor is amorphous (Fig. S2a). The SEM images exhibit a network constructed by a lot of nanowires with a diameter of 20–50 nm (Fig. S2b). After annealing, the amorphous nanowire precursor is transformed to the crystalline $\text{Fe}_2(\text{MoO}_4)_3$ nanoparticles (noted as FMO-M). Finally, graphene wrapped $\text{Fe}_2(\text{MoO}_4)_3$ nanoparticle composite (noted as FMO-MG) was obtained by a physical mixing process of $\text{Fe}_2(\text{MoO}_4)_3$ nanoparticles and graphene. For comparison, a control sample was also synthesized by the hydrothermal process (noted as FMO-H).

To identify the crystallographic phase of the final products, XRD patterns of the as-prepared FMO-H, FMO-M, and FMO-MG are tested (shown in Fig. 2a). All the diffraction peaks in each pattern are indexed to the monoclinic $\text{Fe}_2(\text{MoO}_4)_3$ (JCPDS card No. 00-031-0642). The SEM images of FMO-H in Fig. 2b show micro-spheres assembled by many micro-sheets. The morphologies and the sphere sizes of the hydrothermal samples are similar to some previous works [22,26]. The FMO-M is composed of nanoparticles with a diameter of about 100 nm (Fig. 2c). These nanoparticles are obtained from the fracture and crystallization of the nanowire precursor during annealing

process. The size of the nanoparticles remains unchanged after graphene wrapping (Fig. 2d), and the SEM images of pure graphene used in this work are shown in Fig. S3. Furthermore, the TEM image of FMO-MG (Fig. 2e) shows a direct look on the morphology of the nanoparticles wrapped by graphene, and the lattice spacings of 2.96 and 3.87 Å exhibited by the HRTEM image (Fig. 2f) are in agreement with the (-505) and (-114) planes of $\text{Fe}_2(\text{MoO}_4)_3$, respectively. To further confirm the elemental distribution, EDS-mapping of FMO-MG was measured (Fig. 2g), and it is obvious that C, Fe, Mo and O are uniformly distributed in FMO-MG.

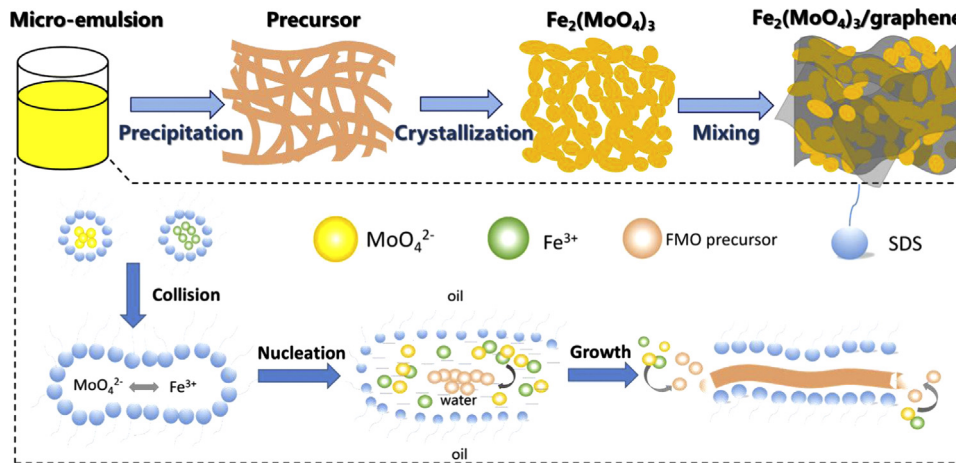


Fig. 1. Schematic illustration of the formation of the $\text{Fe}_2(\text{MoO}_4)_3/\text{graphene}$ composite.

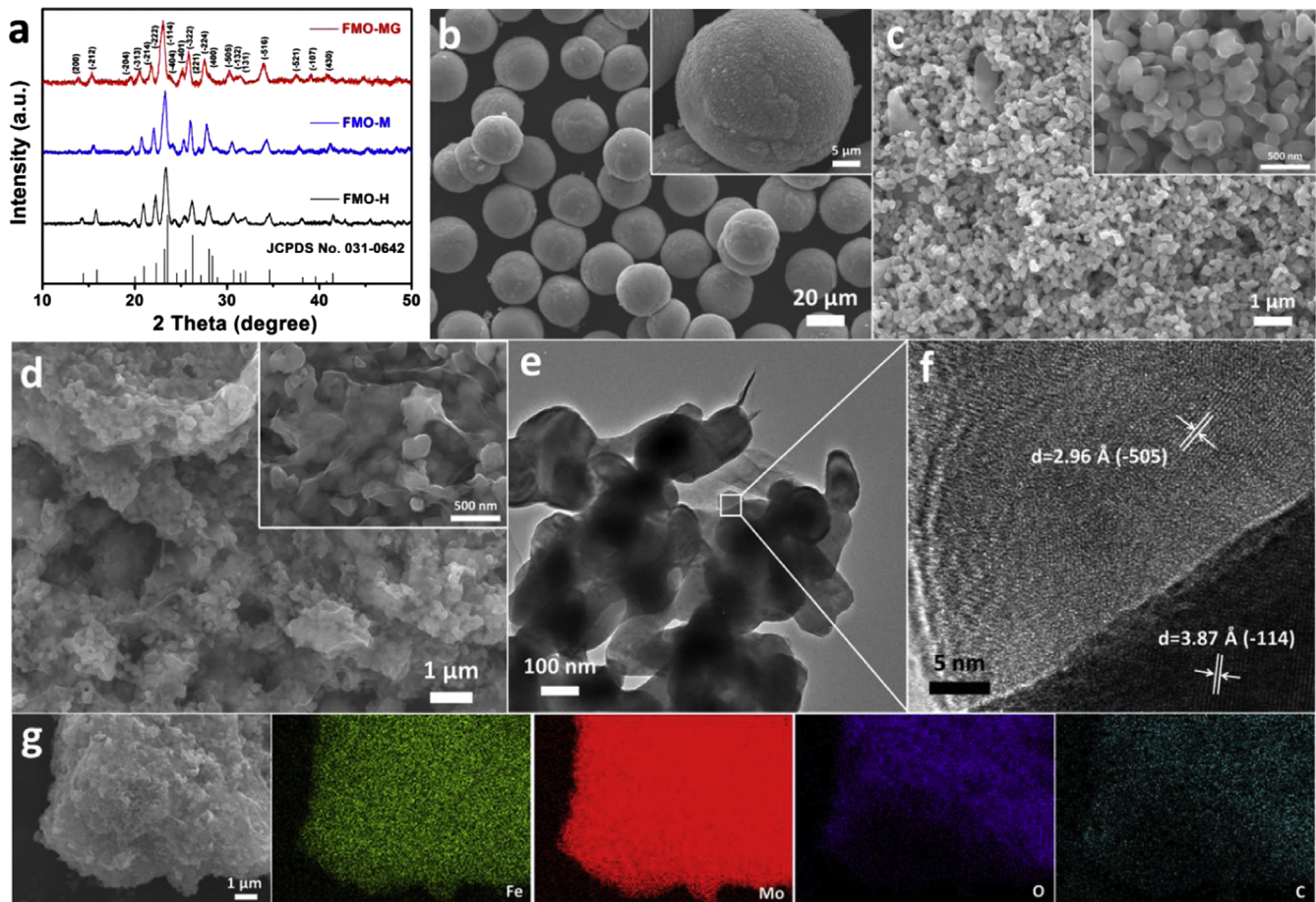


Fig. 2. (a) XRD patterns of FMO-H, FMO-M and FMO-MG; SEM images of FMO-H (b), FMO-M (c) and FMO-MG (d); TEM (e) and HRTEM (f) images of FMO-MG; (g) EDS-mapping of FMO-MG.

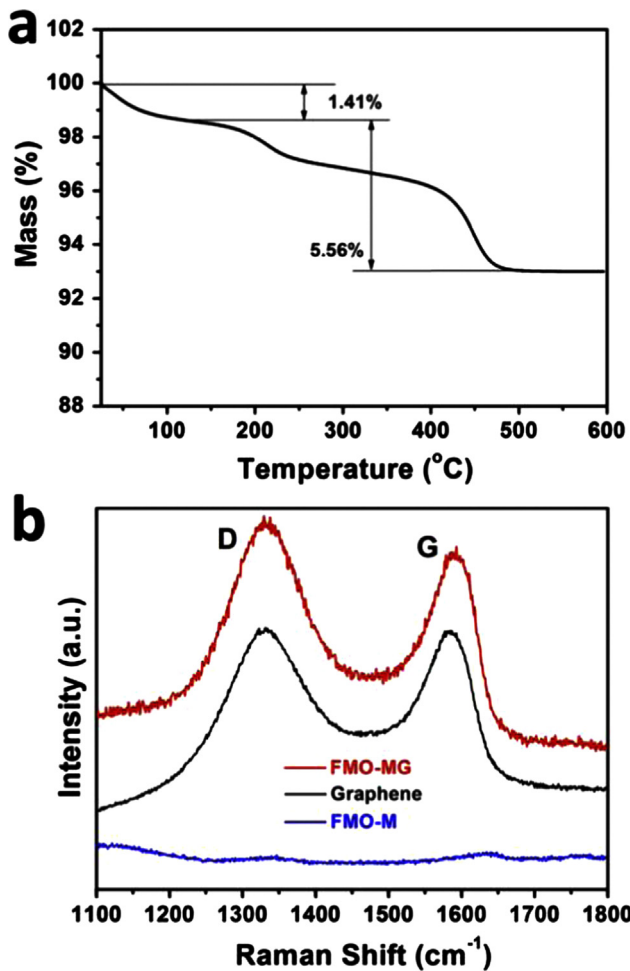
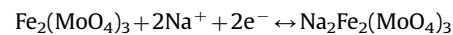


Fig. 3. (a) TG curve of FMO-MG; (b) Raman spectra of FMO-MG, pure graphene and FMO-M.

The TG curve (Fig. 3a) of FMO-MG exhibits two mass loss steps. The first step up to 120 °C is attributed to the removal of 1.41 wt% absorbed water in the material. The second step up to 500 °C is caused by the oxidation of graphene, indicating that the carbon content is 5.56 wt% [40–41]. The mass loss of graphene is lower than the additive amount, because some excess graphene failed to be wrapped on FMO during stirring and centrifuging. Furthermore, Raman spectra are tested to verify the existence of graphene in FMO-MG (Fig. 3b). The bands in the range of 1200–1450 cm^{-1} and 1500–1650 cm^{-1} are attributed to the D-band (K-point phonons of A_{1g} symmetry) and G-band (E_{2g} phonons of C sp^2 atoms) of graphene, respectively [42]. And no obvious peak can be observed in the spectrum of FMO-M, further indicating the existence of graphene in FMO-MG. Nitrogen adsorption–desorption isotherms are further measured to characterize the porous structure of the samples (Figure S4). The Brunauer–Emmerr–Teller (BET) surface areas of FMO-M and FMO-MG are 13.4 $\text{m}^2 \text{g}^{-1}$ and 22.7 $\text{m}^2 \text{g}^{-1}$, respectively, which are larger than that of FMO-H (5.0 $\text{m}^2 \text{g}^{-1}$).

Coin cells with metallic sodium as an anode were assembled to investigate the electrochemical performances of FMO-MG. Fig. 4a shows the cyclic voltammetry of FMO-MG electrode in a voltage window between 1.5 and 4.0 V at a scan rate of 0.1 mV s^{-1} . The cathodic peaks at 2.48 and 2.60 V are corresponded to the phase transformations from $\text{Fe}_2(\text{MoO}_4)_3$ to $\text{Na}_2\text{Fe}_2(\text{MoO}_4)_3$, and the anodic peaks at 2.69 and 2.76 V are corresponded to the phase transformations from $\text{Na}_2\text{Fe}_2(\text{MoO}_4)_3$ back to $\text{Fe}_2(\text{MoO}_4)_3$ [21]. The EDS-mapping of the electrode made by FMO-MG after discharged to 1.5 V also proves the Na^+ intercalation into $\text{Fe}_2(\text{MoO}_4)_3$ (Fig. S5). The electrochemical reaction of $\text{Fe}_2(\text{MoO}_4)_3$ can be described by the following equation [21].



According to Eq. (S1) (exhibited in the supporting information), its theoretical capacity is calculated to be $\sim 91 \text{ mA h g}^{-1}$ corresponding to the charge transfer of 2 e^- per unit formula. Then, the cycling performances of all the three samples at 2 C are displayed

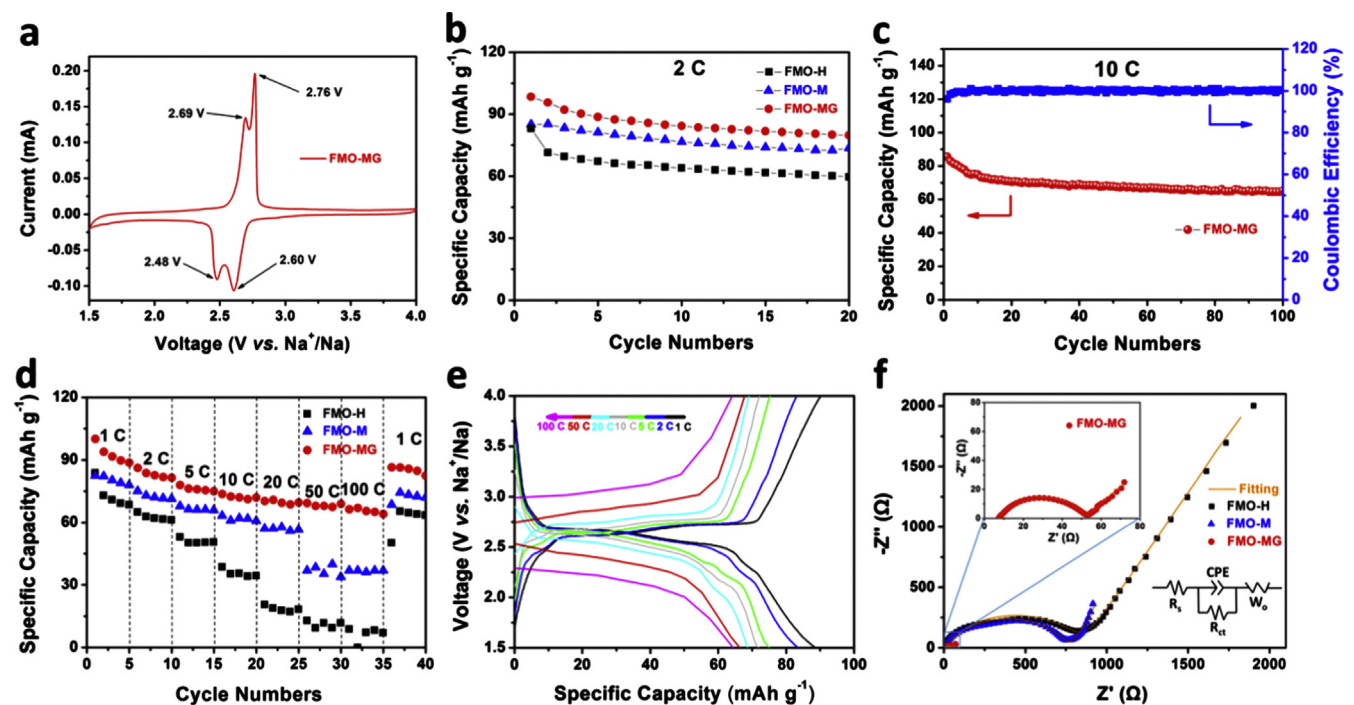


Fig. 4. (a) Cyclic voltammogram curve of FMO-MG at a scan rate of 0.1 mV s^{-1} ; (b) cycling performances of FMO-H, FMO-M and FMO-MG at the rate of 2 C; (c) cycling performance and coulombic efficiency of FMO-MG at the rate of 10 C; (d) rate performances of FMO-H, FMO-M and FMO-MG; (e) charge–discharge curves of FMO-MG at different rates; (f) electrochemical impedance spectra of FMO-H, FMO-M and FMO-MG.

in Fig. 4b. The initial capacity of FMO-MG is 98.4 mA h g^{-1} , which is larger than that of FMO-H and FMO-M (both are $\sim 85 \text{ mA h g}^{-1}$). The capacity of FMO-MG in the initial cycles exceeds the theoretical capacity a little, which can be ascribed to the contribution of capacitive behavior (non-Faradaic electrical double layer capacitance and pseudocapacitance) [9,43]. After charging and discharging for 20 cycles, the capacity of FMO-MG remains 80.4 mA h g^{-1} , while the capacity of FMO-H fades fast in the second cycle. To investigate the reason of the capacity fading of FMO-H, SEM images of the electrode slices made by the three samples before and after 20 cycles are obtained (Fig. S6). Obvious pulverization phenomenon caused by volume expansion during Na^+ intercalation occurs in FMO-H electrode after cycling, while the other two samples maintain their morphology. Therefore, the products with nano-structure exhibit good cycling stability. To further investigate the long-life cycling stability, a galvanostatic charge–discharge measurement of FMO-MG was carried out at a high rate of 10 C (Fig. 4c). A capacity of 65.3 mA h g^{-1} is retained after 100 cycles, corresponding to a capacity retention of more than 76% of the initial capacity. During the cycling process, the coulombic efficiency can maintain at around 100%. The plateaus are clearly observed at 10 C in the charge–discharge curves after 100 cycles (Fig. S7), confirming the high reversibility of FMO-MG even under the high rate. Rate performances of the as-prepared three samples were further evaluated (displayed in Fig. 4d). It is obvious that the capacity of FMO-MG is the highest among the three samples when the rate ranges from 1 C to 100 C. Remarkably, the FMO-MG sample displays a high capacity of 64.1 mA h g^{-1} (64% of the initial capacity) even when the rate reached up to 100 C. The capacity of FMO-H fades to only $\sim 10 \text{ mA h g}^{-1}$ at 100 C, while the FMO-M still retains a relatively high capacity ($\sim 40 \text{ mA h g}^{-1}$). It is worth noting that FMO-MG obtains higher rate capability and enhanced cycling stability compared with the $\text{Fe}_2(\text{MoO}_4)_3$ based products reported in previously works (Table S1). The corresponding charge–discharge curves of FMO-MG are given in Fig. 4e. It is obvious that flat voltage plateaus can be observed at $\sim 2.6 \text{ V}$ under low current density, indicating a stable electrochemical reaction process. The voltage plateaus are clearly observed even at ultra-high rate in charge and discharge curves. To further confirm the capacity contribution, gradually increasing voltammetric scan rates were used to calculate and identify the capacitive and diffusion contribution (Fig. S8). From the CV curves of FMO-MG at various rates, the peak current increases with the increasing of scan rate. Meanwhile, the cathodic and anodic peaks shift slightly to lower and higher potentials, respectively, which is attributed to slight electrode polarization. The two large peaks retained completely even at high scan rate, indicating the high reversibility of insertion/extraction of Na^+ . For the calculation, the total current response (i) at a fixed potential (V) can be described as the combination of these two separate mechanisms:

$$i(V) = k_1\nu + k_2\nu^{1/2}$$

where $k_1\nu$ represents the total capacitive contribution, while $k_2\nu^{1/2}$ stands for the contribution of the diffusion-controlled Faradaic intercalation process [9]. The linear plot of $i/\nu^{1/2}$ versus $\nu^{1/2}$ was used to determine k_1 and k_2 . Thus, the diffusion processes and those from capacitive effects can be distinguished. As a result, the diffusion contribution is 90.8% at 0.1 mV s^{-1} , while it decreases to 66% with the increasing of the scan rate to 1.0 mV s^{-1} . These results show that the diffusion charge storage accounts for a significant proportion of the total capacity, particularly at low scan rates, which corresponds well with the result that the capacity of FMO-MG in the initial cycles exceeds the theoretical capacity. In order to explore the reasons for

the enhanced electrochemical performances of FMO-MG compared with that of the other two samples, electrochemical impedance spectra (EIS) were recorded in Fig. 4f. The Nyquist plots indicate that the charge transfer resistance (Rct) of FMO-MG is 45Ω , which is much lower than that of FMO-M (770Ω) and FMO-H (850Ω). The detailed fitting data is exhibited in Table S2. The results indicate that wrapping of graphene effectively reduces the impedance of $\text{Fe}_2(\text{MoO}_4)_3$ nanoparticles, resulting in the enhanced electrochemical performances of FMO-MG.

In addition, to further investigate the effect of the conductive agent amount on the performances, the electrochemical tests of the electrodes prepared by mixing the active materials, acetylene black and PTFE in a weight ratio of 8:1:1 were measured (Fig. S9). A discharge capacity of 60.9 mA h g^{-1} can be obtained at the high rate of 100 C, and the capacity retention is 70.9% after 100 cycles at the rate of 10 C. These results show similar superior performances with the electrodes in the weight ratio of 6:3:1, demonstrating that the enhanced electrochemical performances are not attributed to the relatively high amount of the conductive agent. To confirm that our strategy of compositing conductive material is an effective way to enhance the electrochemical performances of FMO, we synthesized the $\text{Fe}_2(\text{MoO}_4)_3$ /carbon nanotubes sample (FMO-CNTs) using the similar method of FMO-MG. The SEM images (Fig. S10) show that the carbon nanotubes are composited uniformly with the $\text{Fe}_2(\text{MoO}_4)_3$ nanoparticles. Electrochemical performances are shown in Fig. S11. The FMO-CNTs sample retained a capacity of 58.4 mA h g^{-1} after 100 cycles at the rate of 10 C (70% of the initial capacity). Under the rate of 100 C, the FMO-CNTs sample exhibits a capacity of 57.8 mA h g^{-1} . The performances of FMO-CNTs are comparable with that of FMO-MG, owing to that CNTs can also improve the electronic conductivity of $\text{Fe}_2(\text{MoO}_4)_3$ effectively as graphene. In consideration of the similar synthesis method of the $\text{Fe}_2(\text{MoO}_4)_3$ /graphene and $\text{Fe}_2(\text{MoO}_4)_3$ /CNTs, our method of constructing such nanostructure composite is proved to be effective and successful.

The insertion/extraction mechanism of FMO-MG was investigated by *in-situ* XRD technique (Fig. 5a). It is found that the (-222) , (-114) , (211) , (-224) , (400) , (-505) , (-132) , (131) , (-516) , (-521) and (-107) reflections shift towards lower angles during the discharging process, indicating the increase of corresponding lattice distances. The change in unit cell size rather than structure suggests a typical solid solution behavior [44–45]. Subsequently, at the end of charge process, all the reflections shift back to their original positions, indicating a highly reversible expansion/contraction of the crystal structure. To further investigate the mechanism during the electrochemical process, XPS was recorded to elucidate the valence state change of the elements in the FMO-MG electrode during charge/discharge process. When the sample is charged to 4 V, the core binding energy for the Mo $3d_{5/2}$ and $3d_{3/2}$ peaks are observed at ~ 232.7 and $\sim 235.8 \text{ eV}$, respectively, corresponding to the Mo^{6+} (Fig. 5b) [46–47]. The peak positions do not shift after the electrode is discharged to 1.5 V, indicating Mo does not provide charge transfer during the discharging process (Fig. 5d). The peaks for Fe $2p_{3/2}$ and $2p_{1/2}$ located at $\sim 713.9 \text{ eV}$ and $\sim 724.3 \text{ eV}$ can be associated with the oxidation degree of Fe^{3+} (Fig. 5c) [48–49]. Notably, when the sample is discharged to 1.5 V, the peaks for Fe can be deconvoluted into two peaks at $\sim 713.1 \text{ eV}$ and $\sim 722.9 \text{ eV}$, which can be ascribed to a character of Fe^{2+} (Fig. 5e) [50]. These results demonstrate a $\text{Fe}^{2+}/\text{Fe}^{3+}$ redox couple in the electrochemical process.

To examine the electrochemical kinetics behavior of Na^+ ions in FMO-MG, the diffusion coefficient of Na^+ (D_{Na^+}) was estimated using the galvanostatic intermittent titration technique (GITT), which is a reliable electrochemical technique to calculate diffusivities of ions in electrodes. As shown in Fig. 6a, the GITT data of the second cycle discharging were collected with a current density

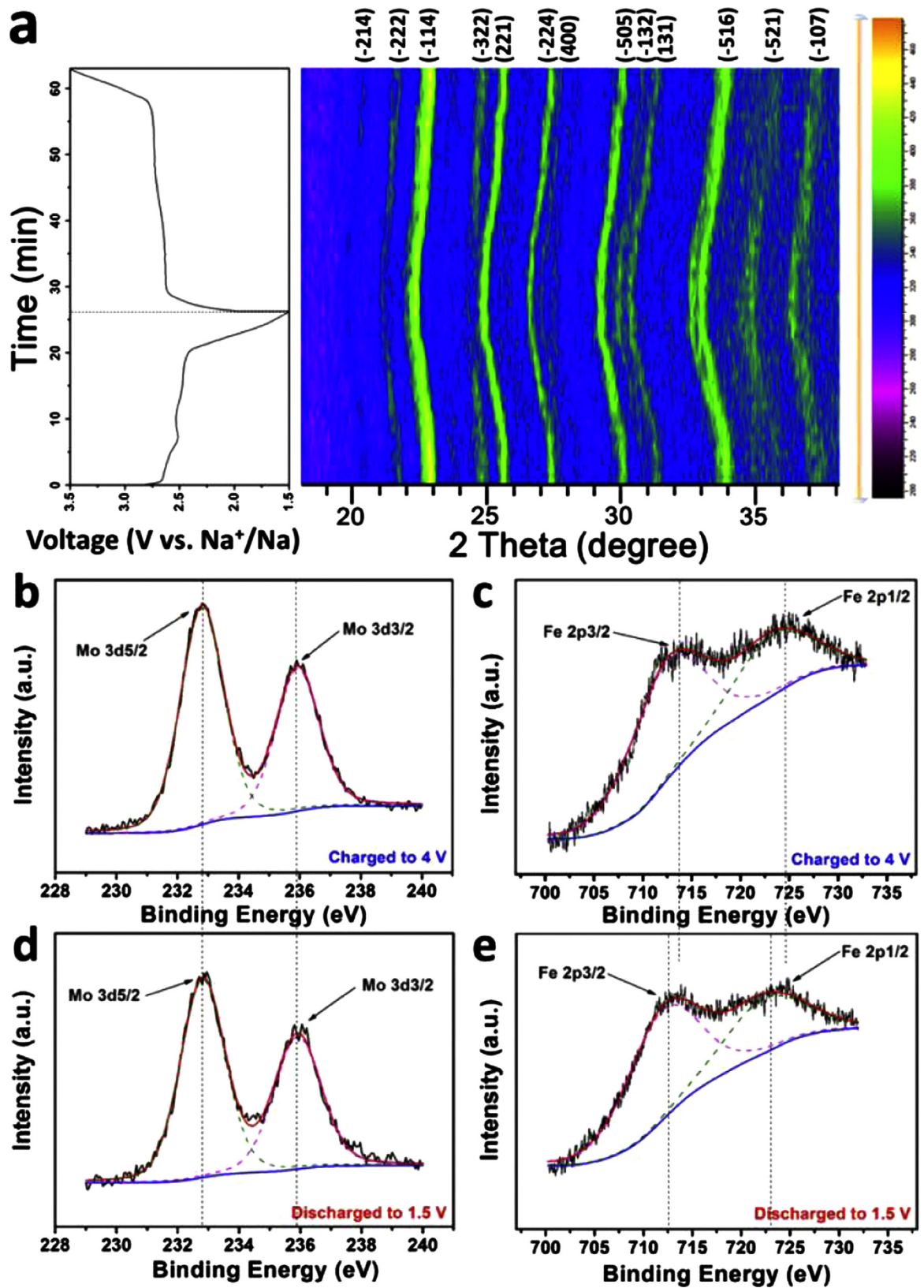


Fig. 5. (a) *In situ* XRD measurement of FMO-MG during the first cycle; (b–e) X-ray photoelectron spectra of FMO-MG in the charged and discharged states; curve fitting for Mo 3d (b) and Fe 2p (c) when the cell is charged to 4 V; curve fitting for Mo 3d (d) and Fe 2p (e) when the cell is discharged to 1.5 V.

of 10 mA g⁻¹ in an interval of 10 min, interrupted by a relaxation for 40 min to get its steady-state voltages. On the basis of Fick's second law, the diffusion coefficient of Na⁺ could be calculated using the equation below [51–54].

$$\tilde{D}_{\text{Na}^+} = 4/\pi \left(\frac{m_B V_M}{M_B A} \right)^2 \left(\frac{\Delta E_s}{\tau \left(\frac{dE_x}{d\sqrt{t}} \right)} \right)^2 \quad (\tau \ll L^2/\tilde{D}_{\text{Na}^+})$$

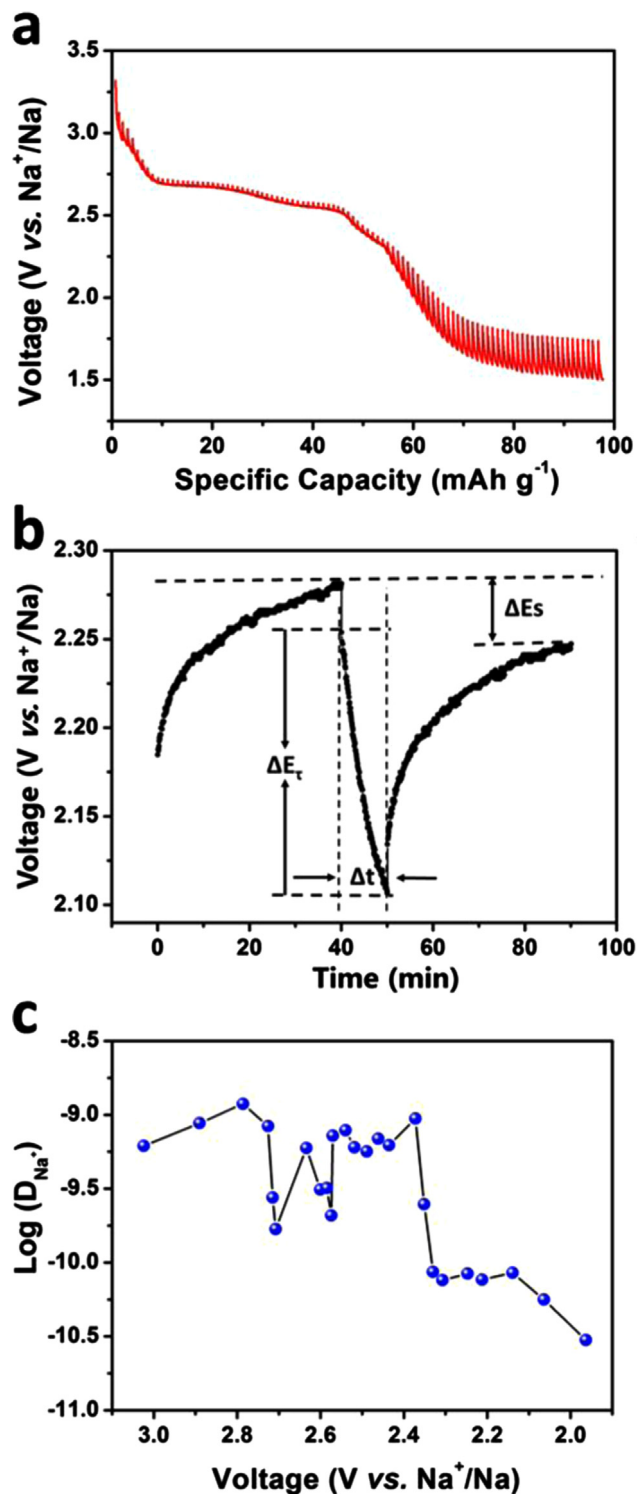


Fig. 6. (a) GITT curve of FMO-MG in the second discharge; (b) demonstration of a single titration during GITT measurement; (c) diffusivity versus state of discharge.

l represents the thickness of the electrode material. m_B and M_B are the mass and the molecular weight. V_M is the molar volume of the compound. S represents the active surface area. τ is the time period of current pulse. $dE_\tau/d(\tau^{1/2})$ is the derivative of the voltage change during the current pulse with respect to the charge or discharge time τ . ΔE_τ is the total change of cell voltage during a constant current pulse, and ΔE_s is the change of the steady-state voltage at the end of the relaxation period over a single galvanostatic titration (Fig. 6b). The D_{Na^+} as a function of voltage curve

(Fig. 6c) is calculated based on the GITT curve for the FMO-MG. The decay of diffusion coefficient in the discharge process can be ascribed to the decreased number of vacant sites with the insertion of sodium in the electrode [51]. D_{Na^+} shows a slight local minimum at 2.5–2.7 V, which is corresponding to the voltage plateaus. This is likely due to an order-disorder phase transition for intercalation of ions, similar to previous reports on materials with a solid solution reaction such as Li_xCoO_2 [52–53]. In the discharge process, the D_{Na^+} value is determined to be 1.187×10^{-9} to $8.64 \times 10^{-11} \text{ cm}^2 \text{ s}^{-1}$, which is much higher than that of the promising electrode material $Na_3V_2(PO_4)_3$ (10^{-12} to $10^{-14} \text{ cm}^2 \text{ s}^{-1}$) calculated from GITT [54].

The FMO-MG composite shows better electrochemical performances than the other two samples, which can be attributed to the following advantages of this material. Firstly, the unique NASICON crystal structure provides an advantaged condition for Na⁺ diffusion. Secondly, the nano-structure provides much larger surface contact area between the electrode and the electrolyte, and drastically shortens the diffusion path of Na⁺. Thirdly, the graphene as a conductive agent provides a conductive network for electronic transport, improving the electrical conductivity of the electrode. The fast ion diffusion coefficient cooperating with the reduced electronic transmission impedance ensures the superior electrochemical performances of the graphene wrapped $Fe_2(MoO_4)_3$ nanoparticle composite. The advantageous NASICON structure, the flat plateaus and the environmental friendliness of $Fe_2(MoO_4)_3$ make it a promising candidate cathode material for sodium ion battery. The high rate performance is also very attractive for its application especially on electric vehicles. Though further effort is needed to improve its performances, it is believe that $Fe_2(MoO_4)_3$ is very valuable to be investigated.

4. Conclusion

In summary, the graphene wrapped $Fe_2(MoO_4)_3$ nanoparticle composite has been synthesized via a facile method, and exhibits a considerable capacity of 98.4 mA h g^{-1} with a flat voltage plateau as a cathode material for SIBs. Remarkably, a relatively high capacity of 64.1 mA h g^{-1} can be obtained under the ultra-high rate of 100 C. The fast ion diffusion coefficient cooperating with the reduced electronic transmission impedance ensures the superior electrochemical performances of the graphene wrapped $Fe_2(MoO_4)_3$ nanoparticle electrode. Furthermore, the Na ion insertion/extraction mechanism of the composite is systematically investigated, based on *in-situ* XRD and XPS. The results above indicate that the graphene wrapped $Fe_2(MoO_4)_3$ nanoparticle composite is a promising cathode material for sodium ion batteries.

Acknowledgments

This work was supported by the National Basic Research Program of China (2013CB934103, 2012CB933003), the International Science & Technology Cooperation Program of China (2013DFA50840), the National Natural Science Foundation of China (51521001, 51272197), the National Natural Science Fund for Distinguished Young Scholars (51425204), the Hubei Provincial Natural Science Fund for Distinguished Young Scholars (2014CFA035), the Fundamental Research Funds for the Central Universities (WUT: 2015-III-021, 2015-III-032, 2015-PY-2), and the Students Innovation and Entrepreneurship Training Program (20151049701034). Thanks to Professor D.Y. Zhao of Fudan University for strong support and stimulating discussion.

Appendix A. Supplementary material

Supplementary data associated with this article can be found in the online version at <http://dx.doi.org/10.1016/j.nanoen.2016.04.021>.

References

- [1] Y. Liu, Y. Qiao, W. Zhang, Z. Li, X. Ji, L. Miao, L. Yuan, X. Hu, Y. Huang, *Nano Energy* 12 (2015) 386–393.
- [2] V.N. Richard, *Nature* 507 (2014) 26–28.
- [3] K.S. Wook, S.D. Hwa, X. Ma, G. Ceder, K. Kang, *Adv. Energy Mater.* 2 (2012) 710–721.
- [4] H. Pan, Y. Hu, L. Chen, *Energy Environ. Sci.* 6 (2013) 2338–2360.
- [5] M.D. Slater, D. Kim, E. Lee, C.S. Johnson, *Adv. Funct. Mater.* 23 (2013) 947–958.
- [6] K. Zhang, Z. Hu, X. Liu, Z. Tao, J. Chen, *Adv. Mater.* 27 (2015) 3305–3309.
- [7] Z. Jian, W. Luo, X. Ji, *J. Am. Chem. Soc.* 137 (2015) 11566–11569.
- [8] X. Lu, G. Xia, J.P. Lemmon, Z. Yang, *J. Power Sources* 195 (2010) 2431–2442.
- [9] Q. Wei, J. Liu, W. Feng, J. Sheng, X. Tian, L. He, Q. An, L. Mai, *J. Mater. Chem. A* 3 (2015) 8070–8075.
- [10] M.S. Islam, C.A.J. Fisher, *Chem. Soc. Rev.* 43 (2014) 185–204.
- [11] S. Li, Y. Dong, L. Xu, X. Xu, L. He, L. Mai, *Adv. Mater.* 26 (2014) 3545–3553.
- [12] Y. Fang, L. Xiao, J. Qian, X. Ai, H. Yang, Y. Cao, *Nano Lett.* 14 (2014) 3539–3543.
- [13] Y. Fang, Q. Liu, L. Xiao, X. Ai, H. Yang, Y. Cao, *A.C.S. Appl. Mater. Interfaces* 7 (2015) 17977–17984.
- [14] J. Ding, Y. Zhou, Q. Sun, X. Yu, X. Yang, Z. Fu, *Electrochim. Acta* 87 (2013) 388–393.
- [15] B.V.R. Reddy, R. Ravikumar, C. Nithya, S. Gopukumar, *J. Mater. Chem. A* 3 (2015) 18059–18063.
- [16] Y. Zhu, Y. Xu, Y. Liu, C. Luo, C. Wang, *Nanoscale* 5 (2012) 780–787.
- [17] N. Wongtharom, T. Lee, C. Wang, Y. Wang, J. Chang, *J. Mater. Chem. A* 2 (2014) 5655–5661.
- [18] Y. Fang, L. Xiao, X. Ai, Y. Cao, H. Yang, *Adv. Mater.* 27 (2015) 5895–5900.
- [19] Y. Jiang, L. Zeng, J. Wang, W. Li, F. Pan, Y. Yu, *Nanoscale* 7 (2015) 14723–14729.
- [20] Z. Jian, C. Yuan, W. Han, X. Lu, L. Gu, X. Xi, Y. Hu, H. Li, W. Chen, D. Chen, Y. Ikuhara, L. Chen, *Adv. Funct. Mater.* 24 (2014) 4265–4272.
- [21] Q. Sun, Q. Ren, Z. Fu, *Electrochem. Commun.* 23 (2012) 145–148.
- [22] J. Yue, Y. Zhou, S. Shi, Z. Shadik, X. Huang, J. Luo, Z. Yang, H. Li, L. Gu, X. Yang, *Sci. Rep.* 5 (2015) 8810.
- [23] V. Nguyen, Y. Liu, X. Yang, W. Chen, *ECS Electrochem. Lett.* 4 (2014) A29–A32.
- [24] V. Nguyen, Y. Liu, Y. Li, S.A. Hakim, X. Yang, W. Chen, *ECS J. Solid State Sci. Technol.* 4 (2015) M25–M29.
- [25] V. Nguyen, Y. Liu, S.A. Hakim, S. Yang, A.R. Radwan, W. Chen, *Int. J. Electrochem. Sci.* 10 (2015) 10565–10575.
- [26] Y. Ding, S. Yu, C. Liu, Z. Zang, *Chem. Eur. J.* 13 (2007) 746–753.
- [27] L. David, R. Bhandavat, G. Singh, *ACS Nano*, 8, (2014) 1759–1770.
- [28] Q. An, F. Lv, Q. Liu, C. Han, K. Zhao, J. Sheng, Q. Wei, M. Yan, L. Mai, *Nano Lett.* 14 (2014) 6250–6256.
- [29] J. Sheng, Q. Li, Q. Wei, P. Zhang, Q. Wang, F. Lv, Q. An, W. Chen, L. Mai, *Nano Res.* 7 (2014) 1604–1612.
- [30] R. Dai, Y. Wang, P. Da, H. Wu, M. Xu, G. Zheng, *Nanoscale* 6 (2014) 13236–13241.
- [31] S. Xu, S. Zhang, J. Zhang, T. Tan, Y. Liu, *J. Mater. Chem. A* 2 (2014) 7221–7228.
- [32] S. Schacht, Q. Huo, I.G. Voigt-Martin, G.D. Stucky, F. Schüth, *Science* 273 (1996) 768–771.
- [33] G.G. Yadav, A. David, H. Zhu, J. Caruthers, Y. Wu, *Nanoscale* 6 (2014) 860–866.
- [34] X. Zhang, F. Cheng, J. Yang, J. Chen, *Nano Lett.* 13 (2013) 2822–2825.
- [35] G.D. Rees, B.H. Robinson, *Adv. Mater.* 5 (1993) 608–619.
- [36] A.K. Ganguli, G. Aparna, V. Sonalika, *Chem. Soc. Rev.* 39 (2010) 474–485.
- [37] Y. Li, C.W. Park, *Langmuir* 15 (1999) 952–956.
- [38] R. Xu, J. Wang, Q. Li, G. Sun, E. Wang, S. Li, J. Gu, M. Ju, *J. Solid State Chem.* 182 (2009) 3177–3182.
- [39] M. Cao, C. Hu, E. Wang, *J. Am. Chem. Soc.* 125 (2003) 11196–11197.
- [40] W. Han, G. Zhao, X. Zhang, S. Zhou, P. Wang, Y. An, B. Xu, *Carbon* 95 (2015) 157–165.
- [41] C. Han, M. Yan, L. Mai, X. Tian, L. Xu, X. Xu, Q. An, Y. Zhao, X. Ma, J. Xie, *Nano Energy* 2 (2013) 916–922.
- [42] C. Botas, P. Álvarez, P. Blanco, M. Granda, C. Blanco, R. Santamaría, L. J. Romasanta, R. Verdejo, M.A. López-Manchado, R. Menéndez, *Carbon* 65 (2013) 156–164.
- [43] P. Simon, Y. Gogotsi, B. Dunn, *Science* 343 (2014) 1210–1211.
- [44] D. Wu, X. Li, B. Xu, N. Twu, L. Liu, G. Ceder, *Energy Environ. Sci.* 8 (2014) 195–202.
- [45] G. He, C.A. Bridges, A. Manthiram, *Chem. Mater.* 27 (2015) 6699–6707.
- [46] M. Anwar, C. Hogarth, R. Bulpitt, *J. Mater. Sci.* 25 (1990) 1784–1788.
- [47] S.L.T. Andersson, R.F. Howe, *J. Phys. Chem.* 93 (1989) 4913–4920.
- [48] D.D. Hawn, B.M. DeKoven, *Surf. Interface Anal.* 10 (1987) 63–74.
- [49] B.J. Tan, K.J. Klabunde, P.M. Sherwood, *Chem. Mater.* 2 (1990) 186–191.
- [50] R.V. Siriwardene, J.M. Cook, *J. Colloid Interface Sci.* 108 (1985) 414–422.
- [51] Y.M. Choi, S.I. Pyun, J.S. Bae, S.I. Moon, *J. Power Sources* 56 (1995) 25–30.
- [52] Y.J. Kim, H. Kim, B. Kim, D. Ahn, J.G. Lee, T.J. Kim, D. Son, J. Cho, Y.W. Kim, B. Park, *Chem. Mater.* 15 (2003) 1505–1511.
- [53] J. Hong, J.R. Selman, *J. Electrochem. Soc.* 147 (2000) 3190–3194.
- [54] Q. Wang, B. Zhao, S. Zhang, X. Gao, C. Deng, *J. Mater. Chem. A* 3 (2015) 7732–7740.



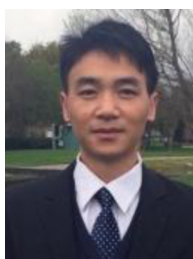
Jinzhi Sheng received his M.S. degree in Materials Engineering from Wuhan University of Technology in 2015. He is currently working toward the Ph.D. degree and his current research focuses on the energy storage materials and devices.



Han Zang is an undergraduate student and in the Department of Materials Science of Engineering from Wuhan University of Technology since 2013. Her current research focuses on nano energy materials and devices.



Chunjuan Tang received her P.H. degree in Chinese Academy of Sciences in 2008. She works in Luoyang Institute of Science and Technology as an associate professor since 2012. Now she is a postdoctor in Wuhan University of Technology, whose interests focus on energy storage.



Qinyou An is Associate Professor of Materials Science and Engineering at Wuhan University of Technology (WUT). He received his Ph.D. degree from WUT in 2014. He carried out his postdoctoral research in the laboratory of Prof. Yan Yao at the University of Houston in 2014–2015. Currently, his research interest includes energy storage materials and devices.



Qjulong Wei received his B.S. degree in Department of Materials Science and Engineering from Wuhan University of Technology in 2011. He is currently working toward the Ph.D. degree. His current research involves the design and synthesis of novel nanomaterials for achieving both high energy density and power density electrochemical energy storage device, including the lithium-ion battery, sodium-ion battery and the hybrid capacitor.



Guobin Zhang received his B.S. degree in Inorganic Non-metallic Materials Engineering from Inner Mongolia University of Science & Technology in 2014 and he is currently working toward the Master. degree. His current research interests include nanomaterials for Li-ions batteries, supercapacitors, sodium batteries and in-situ characterization.



Chen Peng is an undergraduate student and in the Department of Materials Science of Engineering from Wuhan University of Technology since 2014. His current research focuses on nano energy materials and devices.



Lineng Chen received her B.S. degree in College of Materials and Chemistry & Chemical Engineering from Chengdu University of Technology in 2015. She is currently working toward the Ph.D. degree and her current research focuses on Zinc ion batteries, supercapacitors and in-situ characterization.



Liqiang Mai is Chair Professor of Materials Science and Engineering at Wuhan University of Technology (WUT). He received his Ph.D. from WUT in 2004. He carried out his postdoctoral research in the laboratory of Prof. Zhonglin Wang at Georgia Institute of Technology in 2006–2007 and worked as advanced research scholar in the laboratory of Prof. Charles M. Lieber at Harvard University in 2008–2011. His current research interests focus on nanowire materials and devices for energy storage. He received the National Natural Science Fund for Distinguished Young Scholars, the First Prize for Hubei Natural Science Award and so forth.